Numerical Analysis of Rotor Aero-acoustic Characteristics for Ice Detection based on HMB Solver

Xi Chen
Ph.D student
Nanjing University of Aeronautics and Astronautics
Nanjing, China

Qijun Zhao
Professor
Nanjing University of Aeronautics and Astronautics
Nanjing, China

George Barakos
Professor
University of Glasgow
Glasgow, United Kingdom

ABSTRACT

In this work, iced rotors are studied to develop insight in the potential of acoustics-based ice detection. Based on the HMB CFD solver, approximate iced shapes are used and results are analyzed using the FW-H method. Several candidate monitoring positions are assessed for acoustic sensors to be placed on the helicopter fuselage. The influence of ice on the aero-acoustic characteristics of a rotor is calculated, and parameters such as the ice amount and the icing position on the blade are quantified.

NOMENCLATURE

c_0	=sound speed in quiescent medium
ρ_0	=air density
p	=acoustic pressure
p_T	=acoustic pressure due to thickness
p_L	=acoustic pressure due to loading
v_n	=the normal velocity of the surface
$\dot{v}_n$	=the derivative of v_n respect to time
Ma	=local rotational Mach number
Ma_r	=local rotational Mach number in the radiation direction
$\mathbf{x}$	=observer position
$\mathbf{y}$	=source position
r	$=\lvert\mathbf{x}-\mathbf{y}\rvert$
$\hat{r}_i$	=unit radiation vector
l_i	=force/unit area on the medium
l_r	$= l_i \hat{r}_i$
t	=observer time
s	=surface area of the actual body f=0

Subscripts

ret	=quantity evaluated at retarded time

INTRODUCTION

Helicopter ice accretion, especially on rotors, can be a serious threat to flight safety (Ref. 1) since it modifies the designed aerodynamic shapes and degrades the rotor aerodynamic performance (Ref. 2, 3). At present, there are two main approaches to deal with ice accretion on aircraft (Ref. 4). First, pilots are given complete weather information and try to avoid potential icing conditions. Second, aircraft are thoroughly deiced before take-off and then operate an ice protection system (IPS) to accomplish in-flight ice removal. At present, only 5% of the US rotorcraft are equipped with an IPS (Ref. 5). For helicopters without IPS, the general rule is to avoid flying in icing conditions. Compared to fixed-wing aircraft, helicopter rotor ice accretion is not well understood due to complexities in the 3-D rotor flow environment with inherent unsteady flow, rotational movement of rotor and strong centrifugal forces on the blade (Ref. 6, 7). Perhaps the best defense against icing is early detection since the pilots can make use of the IPS effectively or change their flight plan to avoid operation within icing conditions. For the above reasons, ice detection has become critically important for helicopter safety and efficiency.

Many sensors using different technologies have so far been developed, and employed to detect the ice formation on aircraft surfaces (Ref. 8, 9). An ice detection system consists of a resonant piezoelectric sensing-element and a microprocessor controller, and it can sense ice and water films up to 0.5 mm thick (Ref. 10). Another approach was also investigated, based on scatter of light in the iced volume (Ref. 11). However, these sensors are difficult to deploy due to the limited space inside blades (Ref. 12). In addition, due to the complex motion of rotors, such as rotor flapping, regular ice detection methods like infrared detectors (Ref. 13) are also difficult to implement on rotors.

Presented at the AHS International 74th Annual Forum & Technology Display, Phoenix, Arizona, USA, May 14-17, 2018.

According to previous studies (Ref. 14, 15), the change of the flow behavior and blade shape by ice accretion is likely to affect the helicopter main rotor noise. Cheng's studies (Ref. 16) also show that rotor noise can be used to detect the formation of ice at the early stage of ice accretion. Anyway, there are few other studies of helicopter noise during ice accretion found in the open literature. A noise monitor, such as a microphone array, which does not have to be mounted on the rotor, is easier to deploy on helicopter fuselage, and there is no need for rotor blade modifications. In addition, several works have already been published on the aero-acoustic characteristics on rotors (Ref. 17, 18). These developments make the ice detection by rotor aero-acoustic characteristics possible.

Based on the Helicopter Multi-Block (HMB) CFD code (Ref. 19), the objective of the present work is to analyze the variation of aero-acoustic characteristics of iced rotors, and identify microphone positions that are suitable for detecting ice accretion. The influence of ice on the aero-acoustic characteristics of rotors is first calculated. Then, the effects of the ice amount and the icing position on the blade are evaluated. The sensitivity of the acoustic characteristics to ice accretion is also analyzed, and some microphone positions are suggested.

HELICOPTER MULTI-BLOCK CFD SOLVER

The HMB solver was employed in this work. HMB solves the unsteady Reynolds-averaged Navier-Stokes equations on block-structured grids using a cell centered finite-volume method for spatial discretization. Implicit time integration is employed, and the resulting linear system of equations is solved using a pre-conditioned Generalized Conjugate Gradient method. For unsteady simulations, an implicit dual time stepping method is used. The method has been validated for a wide range of aerospace applications and has demonstrated good accuracy and efficiency for very demanding flows (Ref. 20).

AERODYNAMIC AND ACOUSTIC METHOD

Based on the CFD airloads obtained by the HMB solver, the Ffowcs-Williams Hawkings (FWH) method is used for calculating the aero-acoustic characteristic of clean and iced rotors (Ref. 21). The FWH theory is derived by combining the equations of mass and momentum conservation for compressible fluids, to obtain an inhomogeneous wave equation. This equation governs the generation and propagation of sound waves in a volume outside any closed surface. The Farassat 1A equation to be solved for the FWH is as follows

$$p(\mathbf{x},t) = p_T(\mathbf{x},t) + p_L(\mathbf{x},t) \tag{1}$$

where,

$$4\pi p_T(\mathbf{x},t) = \int_{f=0}\left[\frac{\rho_0 v_n\left(r\dot{M}a_i\hat{r}_i + c_0 Ma_r - c_0 Ma^2\right)}{r^2\left(1-Ma_r\right)^3}\right]_{ret} ds + \int_{f=0}\left[\frac{\rho_0(\dot{v}_n + v_n)}{r\left(1-Ma_r\right)^2}\right]_{ret} ds \tag{2}$$

and

$$4\pi p_L(\mathbf{x},t) = \frac{1}{c_0}\int_{f=0}\left[\frac{\dot{l}_i\hat{r}_i}{r\left(1-Ma_r\right)^2}\right]_{ret} ds + \int_{f=0}\left[\frac{l_r - l_i Ma_i}{r^2\left(1-Ma_r\right)^2}\right]_{ret} ds + \frac{1}{c_0}\int_{f=0}\left[\frac{l_r\left(r\dot{M}a_i\hat{r}_i + c_0 Ma_r - c_0 Ma^2\right)}{r^2\left(1-Ma_r\right)^3}\right]_{ret} ds \tag{3}$$

This foundation is used in the current work.

CALCULATED RESULTS AND ANALYSES

Aerodynamic characteristics on NACA23012 airfoil with and without ice

The experimental data for an iced NACA23012 airfoil, obtained at the NASA Langley Low Turbulence Pressure Tunnel (LTPT) is selected to validate the accuracy of the employed numerical method. The LTPT measurements were at a Mach number of 0.208 and at a Reynolds number of approximately 2×10^6 (Ref. 22).

Figure 1 shows a detailed view of the ice shape and the modified NACA23012 section. The ice amount is very small, and the radius of the ice is only 0.0139c. Figure 2 shows the aerodynamic characteristics of the NACA23012 with and without ice. The comparisons of C_L and C_D with experimental data (Ref. 22) show fair agreement. When ice forms on the airfoil, the lift force decreases, and the drag force increases.

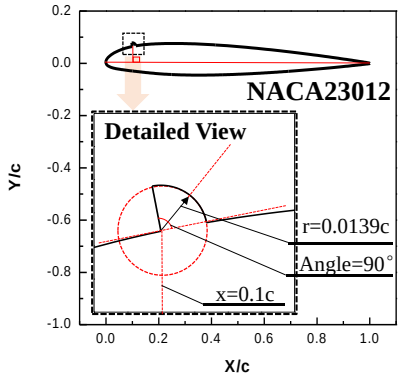

Figure 1. Detailed view of the ice shape and the modified NACA23012 section.

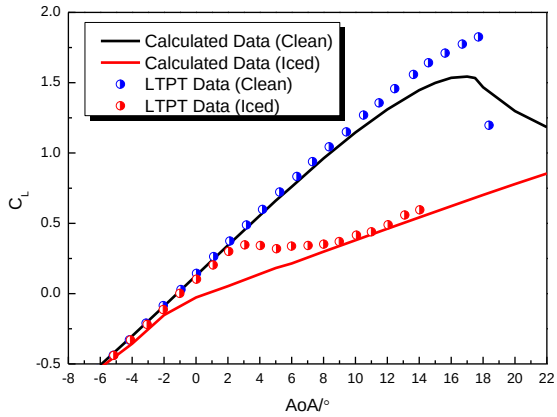

(a) C_L

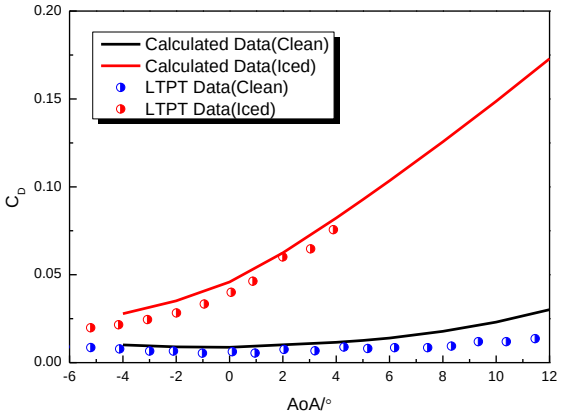

(b) C_D

Figure 2. Aerodynamic characteristics of NACA 23012 airfoil with and without ice.

Figure 3 shows pressure coefficient distributions on the airfoil surface with and without ice, at 0 ° of the angle of attack. As shown, the calculated results are in good agreement with LTPT data, indicating that the present CFD solver is reliable for simulating the aerodynamic characteristics of the iced airfoils.

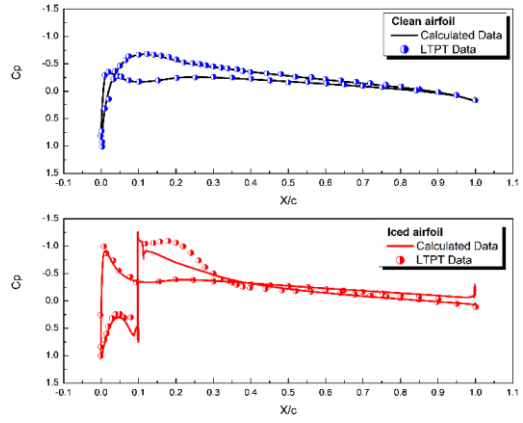

Figure 3. Pressure coefficient distributions of NACA 23012 airfoil with and without ice.

Acoustic characteristics of rotors in hover with and without ice

The Caradonna-Tung (CT) rotor is selected to analyze the variation of acoustic characteristics of iced rotors in hover. The CT rotor has two rectangular blades with a conventional NACA 0012 airfoil. For the iced rotor, the icing positions were from 0.6R to 0.9R along the blade. Figure 4 shows the icing position on the C-T rotor and sectional ice shapes.

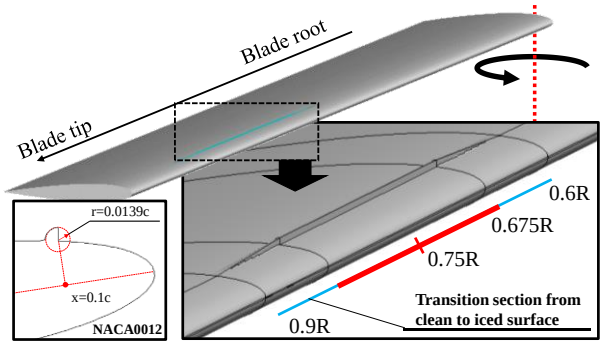

Figure 4. Icing position on the C-T rotor and sectional ice shape

Clean and iced cases for this rotor at M_{tip}=0.794 and at Re=3.48×10^6 were calculated. Table 1 shows the variation of the aerodynamic performance of the rotor in hover with and without ice at a collective pitch of 8 °. In addition, Figure 5 shows the comparison of the sectional pressure distribution of the clean C-T rotor with experiment data. As can be seen, the numerical results are in a good agreement with experiments (Ref. 23).

Table 1. Variation of aerodynamic performance of rotor in hover with and without ice.

Aerodynamic characteristics	C_T	C_Q	FM
Clean Rotor	1.10×10-2	1.17×10-3	0.492
Iced Rotor	0.61×10-2	1.54×10-3	0.156
Variation	-44.1%	+31.5%	-68.2%

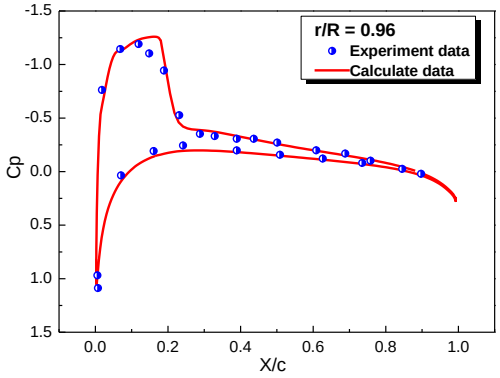

Figure 5. Comparison of the sectional pressure distribution of clean C-T rotor with experiment data.

Although the iced area is small compared with the blade sectional area, the deterioration of the aerodynamic characteristics is obvious, as seen in table 1. There is a decrease of about 70 percent in the figure of merit. This is not only qualifying the strong influence of ice on the rotor aerodynamic performance, but also the importance of ice detection on rotor blades.

Figure 6 shows some monitoring points placed relative to the blade for ice detection. Considering the installation of acoustic monitors on the fuselage, all monitors are below the rotating plate, and their location is defined by the coordinates (r, z).

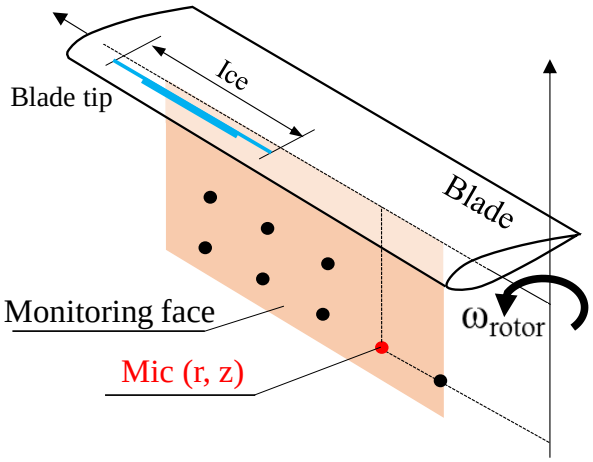

Figure 6. Positions of acoustics monitors relative to the blade.

Figure 7 shows the effective sound pressure at different monitor positions, between clean and iced rotors. There are significant differences in the obtained acoustics. On the z=-0.5R plane, the effective sound pressure of the iced rotor decreases compared with the clean rotor. This is because the lift force of the iced rotor drops. On the z=-0.25R plane, the effective sound pressure of the iced rotor first increases and then decreases compared to the clean rotor near the blade root.

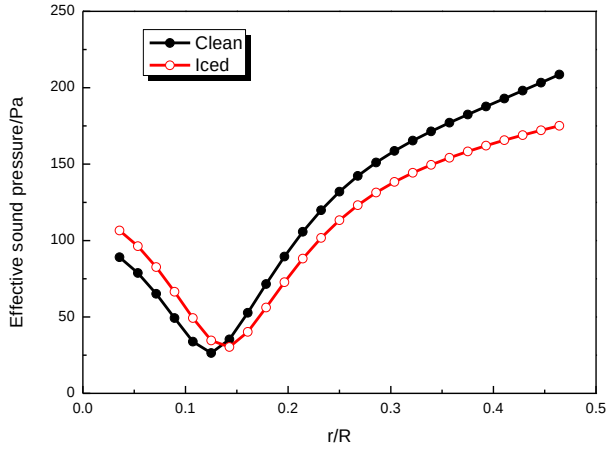

(a) z=-0.25R

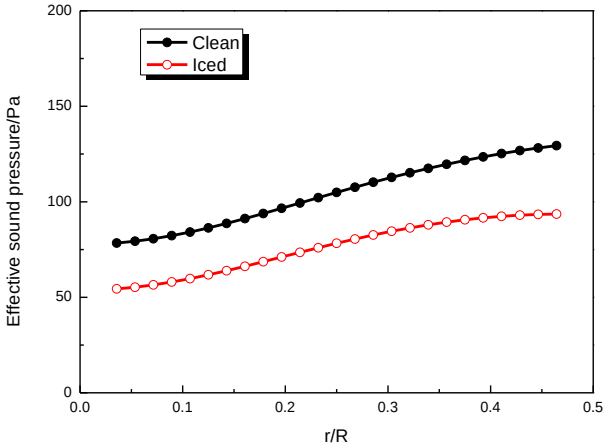

(b) z=-0.5R

Figure 7. Effective sound pressure at different monitor positions for clean and iced rotors

Figure 8 shows the differences of the effective sound pressure at different z planes. When the monitor is far away from the rotor plane, the effective sound pressures of all monitors at the different radial positions decrease. When monitors are close to the rotor plane, the effective sound pressure changes significantly in the radial direction. It increases in places, and decreases in others. However, the variation of sound pressure is evident in this case, indicating that ice can be detected based on the variation of the blade acoustic characteristics.

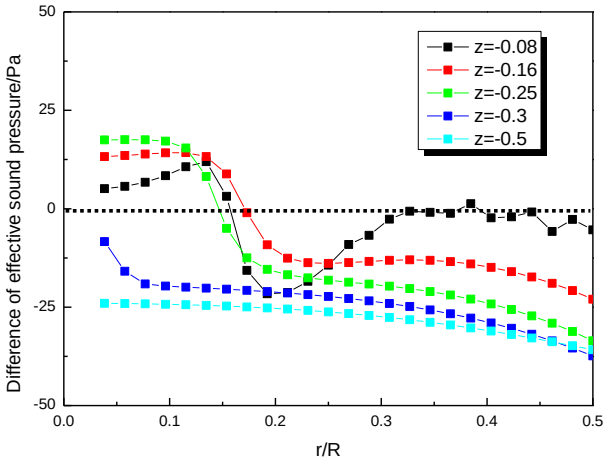

Figure 8. Difference of the effective sound pressure between clean and iced rotors at different z planes

To further analyze the acoustics variations, figure 9 shows the differences of the effective sound pressures at various monitor positions. It is assumed that the acoustic monitor can detect changes in sound pressure bigger than 10 Pa. For this iced rotor, as long as the acoustic monitor is in the yellow or blue region, ice can be detected.

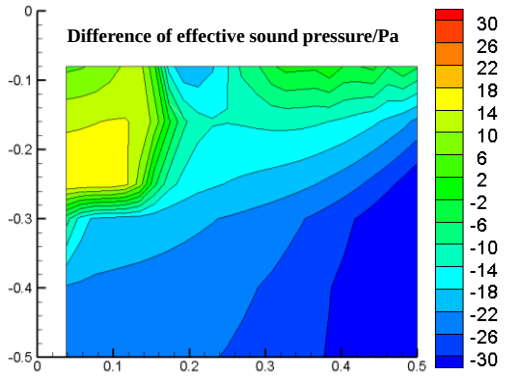

Figure 9. Difference of the effective sound pressure between clean and iced rotors

In addition, the sound pressure time histories of a typical monitoring position (r=0.25R, z=-0.25R) are given in figure 10. The difference in the effective sound pressure for this position is 15 Pa. As can be seen, the main difference of the effective sound pressure comes from loading noise, while the thickness noise is almost unchanged. Considering the large variation of the aerodynamic characteristics in this case, the acoustic characteristics of some iced rotors with shorter ice lengths were also calculated.

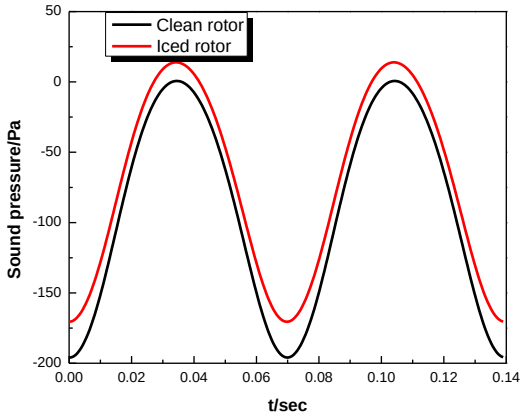

(a) Loading noise

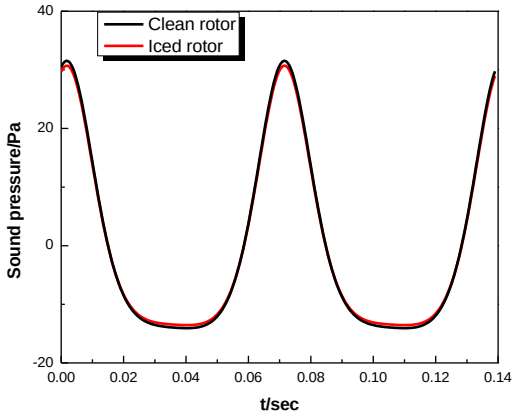

(b) Thickness noise

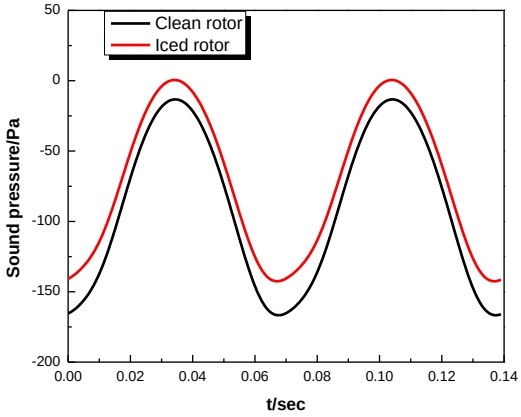

(c) Total noise

Figure 10. Sound pressure time histories at a typical monitoring position

Acoustic characteristics of iced rotor with different ice amount.

Three rotors with different ice lengths are added to analyze the variation of acoustic characteristics, as seen in figure 11. Blade A is the previously used iced rotor, and its ice length is 0.3R. The ice length of rotor D is the shortest, only 0.033R.

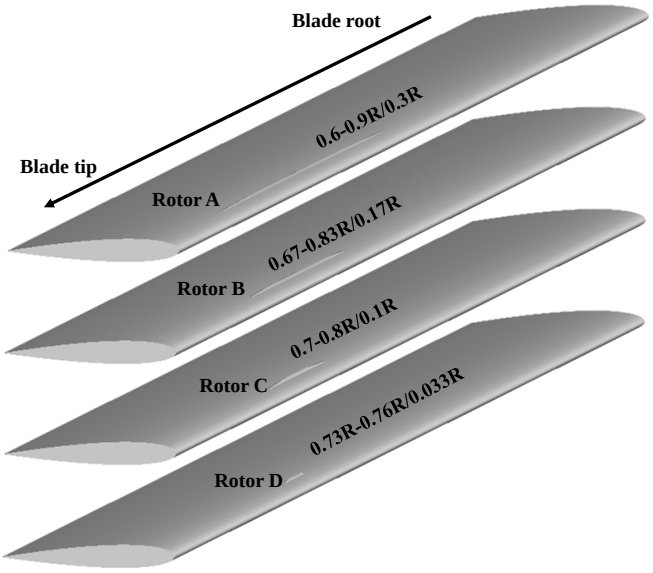

Figure 11. Ice lengths used for analysis.

Table 2 shows the aerodynamic characteristics of the rotors at the same condition, M_{tip}=0.794, Re=3.48×10^6 and for a collective pitch of 8°. With the decrease in the ice length, the variation of aerodynamic characteristics of the rotor decreases. For rotor D, the variation of FM is only 7.69%.

Table 2. Aerodynamic performance of different iced rotors in hover.

Aerodynamic characteristics	C_T	C_Q	FM	Variation of FM
Clean	1.10×10^{-2}	1.17×10^{-3}	0.492	
Rotor A	0.61×10^{-2}	1.54×10^{-3}	0.156	-68.2%
Rotor B	0.91×10^{-2}	1.36×10^{-3}	0.318	-35.4%
Rotor C	1.04×10^{-2}	1.29×10^{-3}	0.409	-16.8%
Rotor D	1.06×10^{-2}	1.21×10^{-3}	0.454	-7.69%

Figure 12 shows the sound pressure time histories of two typical monitoring points (r=0.25R, z=-0.25R and r=0.25R, z=-0.3R). As seen, the sound pressure of rotor A decreases compared with the clean rotor, and the sound pressures of rotors C and D slightly increase. This is more obvious on the z=-0.3R plane, because iced rotors with less ice maintain good aerodynamic characteristics.

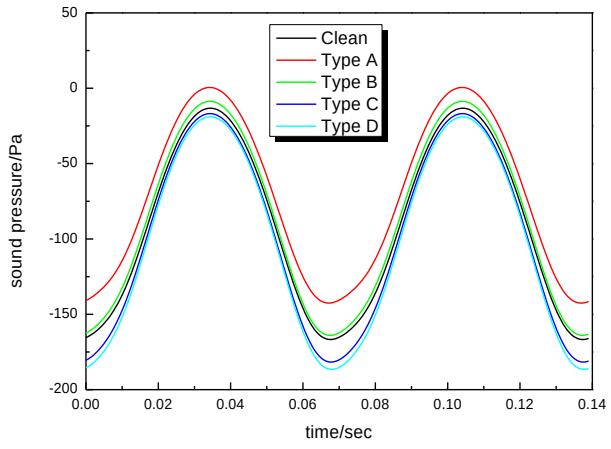

(a) r=0.25R, z=-0.25R

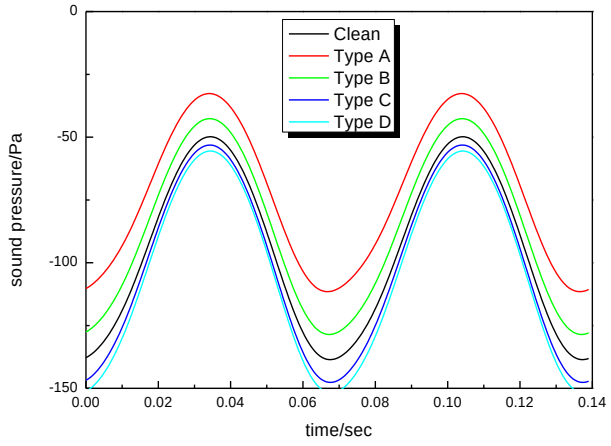

(b) r=0.25R, z=-0.3R

Figure 12. Sound pressure time histories of two typical monitoring positions

Figure 13 shows the effective sound pressure on the z=-0.25R plane, and figure 14 shows the difference of effective sound pressure. When the ice length is small, the effective sound pressure decreases near the blade root and increases near the middle of the blade along the radius.

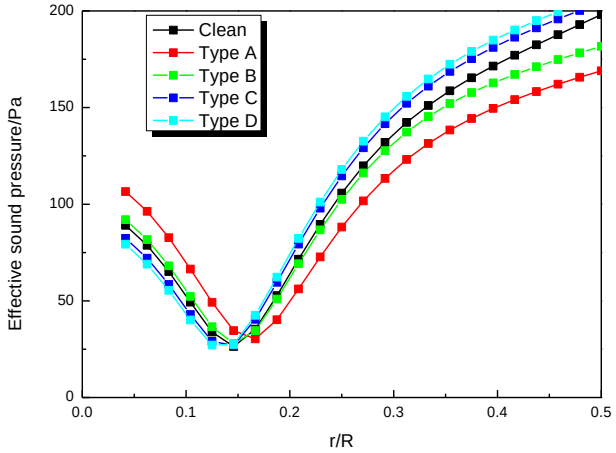

Figure 13. Effective sound pressure with different monitoring positions on the z=-0.25R plane.

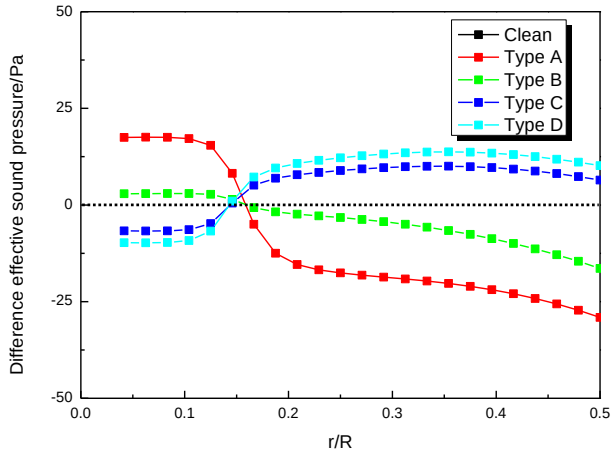

Figure 14. Differences of effective sound pressure on the z=-0.25R plane.

During the early stage of ice accretion, the ice length is normally short. Thus, ice detection for rotors with short ice lengths is more important.

Figure 15 shows the comparison of the effective sound pressures between the clean rotor and the iced rotor D, at different monitor positions. When the monitor is far away from the rotation plane, the effective sound pressure of rotor D is very close to the clean rotor. When the monitor position is close to the rotation plane, the effective sound pressure of the iced rotor first remains nearly constant, and then clearly changes. To show this, the differences of the effective sound pressure at different z planes are given in figure 16.

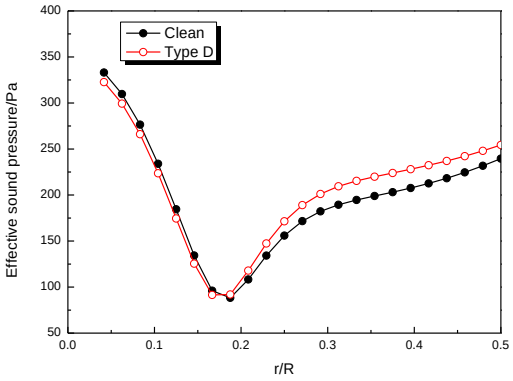

(a) z=-0.16R

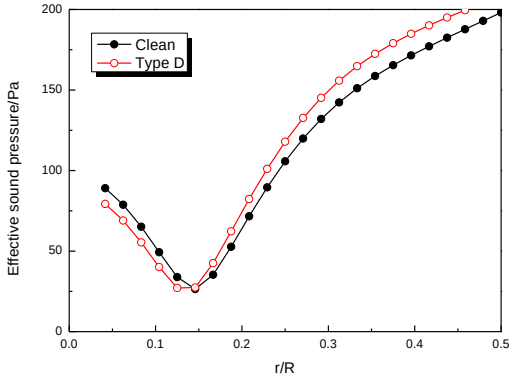

(b) z=-0.25R

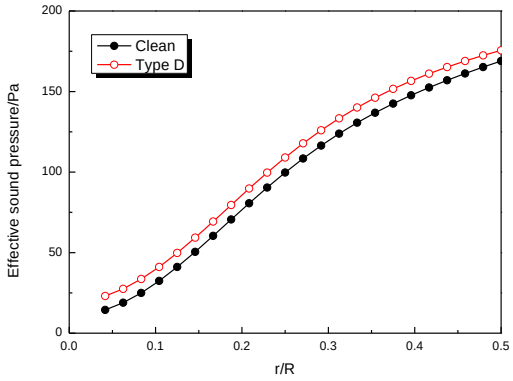

(c) z=-0.3R

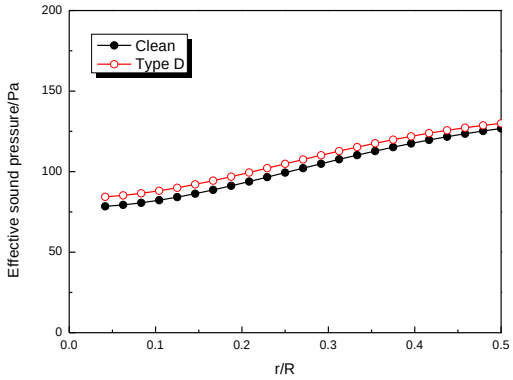

(d) z=-0.5R

Figure 15. Effective sound pressure at different monitor positions between clean rotor and rotor D.

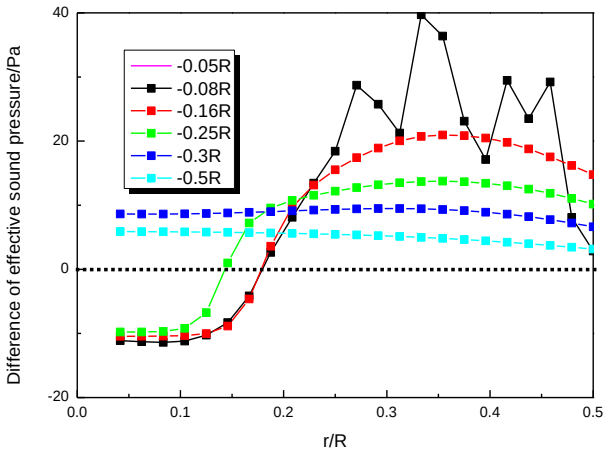

Figure 16. Difference of the effective sound pressure between clean rotor and rotor D, at different z planes.

As seen (figure 16), even if the ice length is very short, the variation of the acoustic characteristics of the rotor is still apparent. This indicates that the small variation of the blade shape, at the early stage of ice accretion, can be detected by the variation of the blade acoustic characteristics.

Figure 17 shows the difference of the effective sound pressure at different monitoring positions for rotor D. In the yellow and green regions, the difference of effective sound pressure is too low, and the acoustic monitor cannot detect the ice. In the red regions, the effective sound pressure increases. As a result, these regions are appropriate for monitor installation. Similarly, the blue region is also a good monitoring area, although the effective sound pressure decreases there.

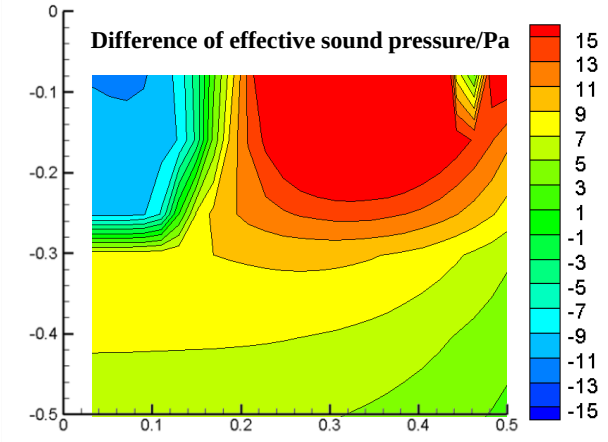

Figure 17. Difference of the effective sound pressure at different monitoring positions between the clean rotor, and rotor D.

Acoustic characteristics of iced rotors with different icing positions.

Two iced rotors with different icing position are added to analyze the influence of the icing position on the acoustic

characteristics, as shown in figure 18. The ice length and ice shape of these two iced rotors are the same as rotor D, the only difference is the icing position. The icing position of rotor E is from 0.53R to 0.56R, and that of rotor F is from 0.33R to 0.36R.

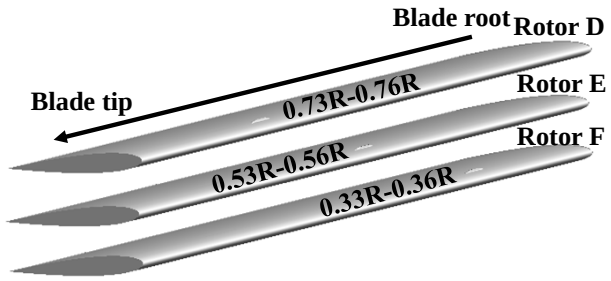

Figure 18. Different icing positions used for analysis.

Table 3 shows the aerodynamic characteristics of the iced rotors at the same condition, M_{tip}=0.794, Re=3.48×10^6 and collective pitch of 8°. With ice moving to the blade root, the variation of the FM decreases. However, the ice accretion has little effect on the aerodynamic characteristics of these three rotors.

Table 3. Aerodynamic performance of different iced rotors in hover.

Aerodynamic characteristics	C_T	C_Q	FM	Variation of FM
Clean	1.10×10^{-2}	1.17×10^{-3}	0.492	
Rotor D	1.06×10^{-2}	1.21×10^{-3}	0.454	-7.69%
Rotor E	1.07×10^{-2}	1.20×10^{-3}	0.461	-6.31%
Rotor F	1.07×10^{-2}	1.18×10^{-3}	0.468	-4.87%

Figure 19 shows the effective sound pressure of different iced rotors below the rotor plane.

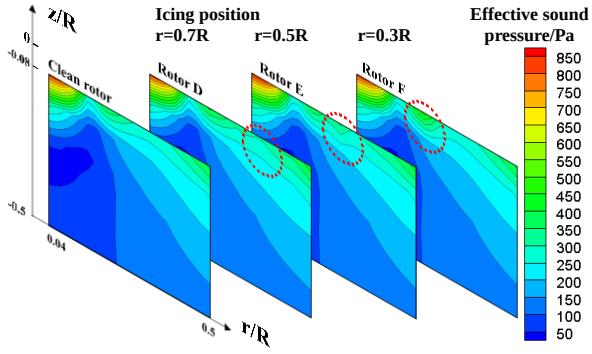

Figure 19. The effective sound pressure of different iced rotors below the rotor plane in hover.

Since the ice amounts on rotors E and F are very small, the changes of the effective sound pressures are not appreciable. However, the influence of the icing position on the effective sound pressure of the rotor is clear, as shown in the figure.

Figure 20 shows the differences of the effective sound pressures between iced and clean rotors. For rotor E, the obvious variation area (differences greater than 5 or less than 5 Pa) is from r=0.1R to r=0.42R along the radial direction and near the z=-0.15 plane. For rotor F, the obvious variation area is from r=0.1R to r=0.3R along the radial direction and near the z=-0.2 plane. Combining with figure 17, ice can change the effective sound pressure in a limited area, and this area is from the blade root to the icing position along the radial direction.

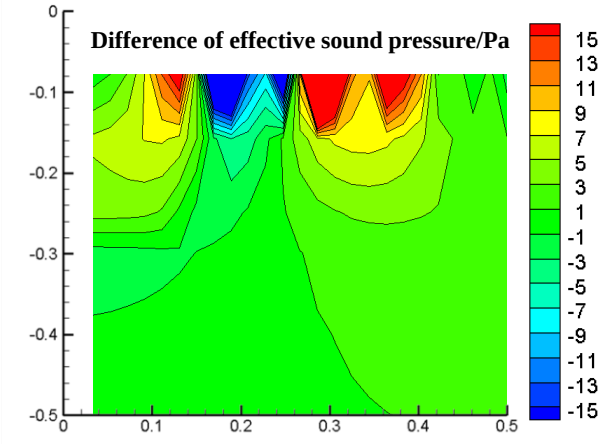

(a) Rotor E

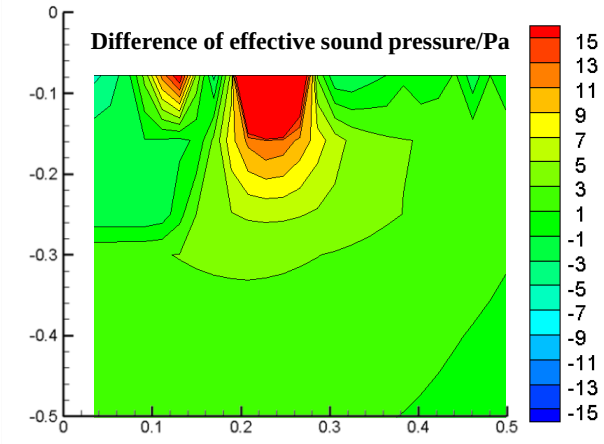

(b) Rotor F

Figure 20. The difference of effective sound pressure between iced rotors and clean rotor.

For comparison purposes, the absolute values of the differences in the effective sound pressure between these iced rotors and the clean rotor on the z=-0.16R plane are given in figure 21. As can be seen, when the icing position is closer to the blade tip, such as for rotor D, the region of the effective sound pressure variation is larger. When the icing position is closer to the blade root, such as for rotor F, the region of the effective sound pressure variation is small.

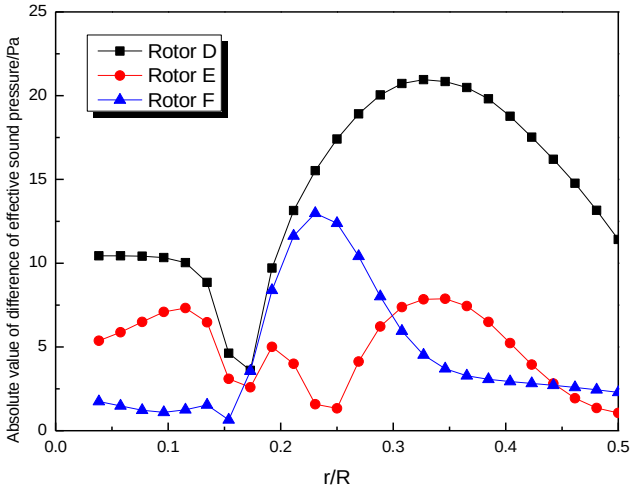

Figure 21. The absolute values of the differences in the effective sound pressure between these iced rotors and the clean rotor on the z=-0.16R plane

In addition, the comparison of the total sound pressure time histories at four monitoring positions on the z=-0.16R plane are given in figure 22. At r=0.1R, the sound pressure time histories of rotor F and the clean rotor are nearly the same, while there are obvious changes for rotors D and E. Then, the changes for rotor F are evident at r=0.2R, and decrease at r=0.3R. There are no appreciable differences between rotor F and the clean rotor.

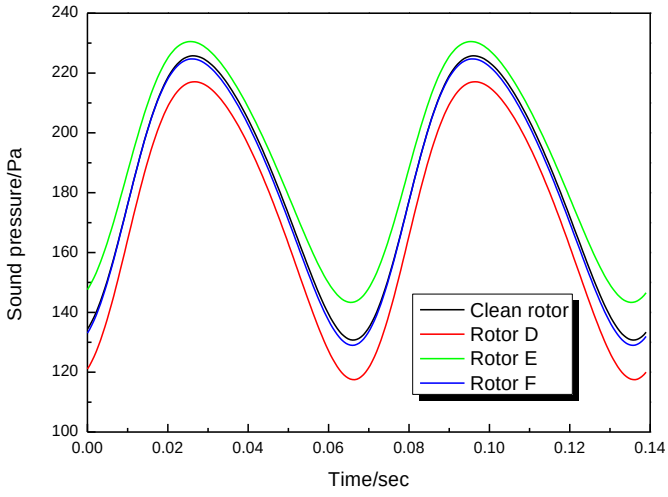

(a) r=0.1R

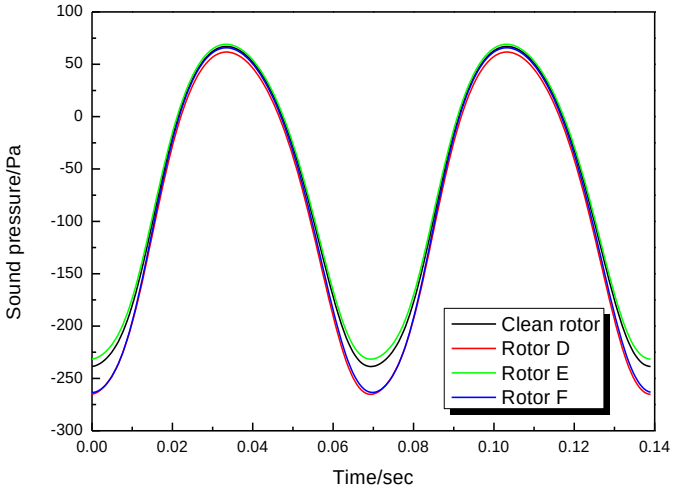

(b) r=0.2R

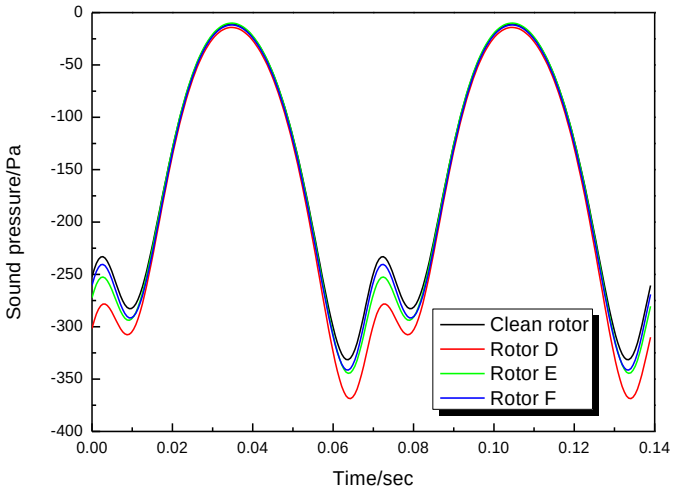

(c) r=0.3R

Figure 22. The comparison of total sound pressure time histories at four monitoring positions on the z=-0.16R plane

As a result, through the variations of the sound pressure at different monitoring points, the icing position on rotors can be detected, especially if several monitors are used.

Acoustic characteristics of a rotor in forward flight with a short ice shape

Based on the above analysis, UH-60A rotors with and without ice are computed in forward flight. The ice length is very short, and it is only 0.012R. The iced region is from 0.594R to 0.606R, as shown in figure 23.

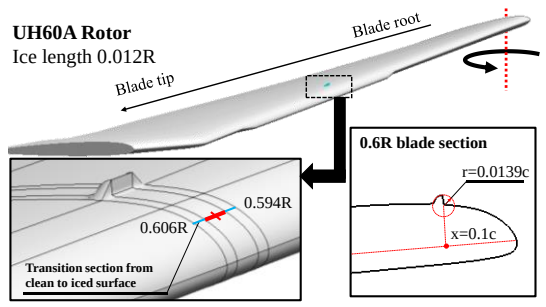

Figure 23. Icing position on the UH-60A rotor and sectional ice shape

Clean and iced rotors at M_{tip}=0.642 and μ=0.368 were calculated. Figure 24 shows the comparison of the sectional lift coefficients of the clean rotor with experiment data. As can be seen, the numerical results are in good agreement with experiments.

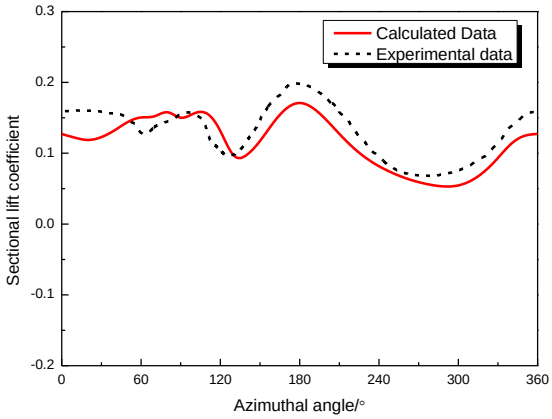

(a) r=0.675R

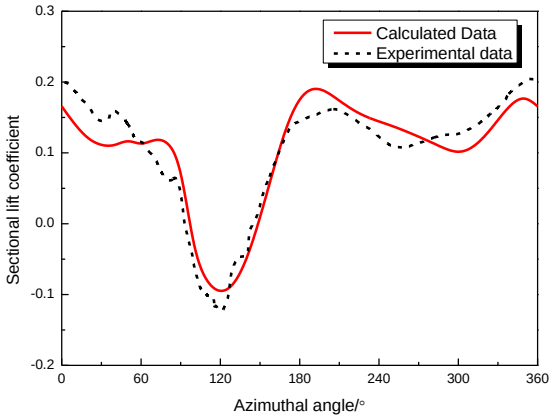

(b) r=0.865R

Figure 24. Sectional lift coefficient of the UH-60A rotor in forward flight

Figure 25 shows comparisons of sectional lift coefficients between the clean and iced rotors. At r=0.6R (near the icing area), there is an obvious difference in the range from 60 ° to 120 ° of azimuth angles. However, at r=0.5R and r=0.7R, there are no appreciable differences between the iced and clean rotors. This means that the loading differences are too small for the overall rotor, and the short ice shape has little effect on the aerodynamic characteristics. So, in this case, ice is difficult to be detected by the variation of the aerodynamic characteristics.

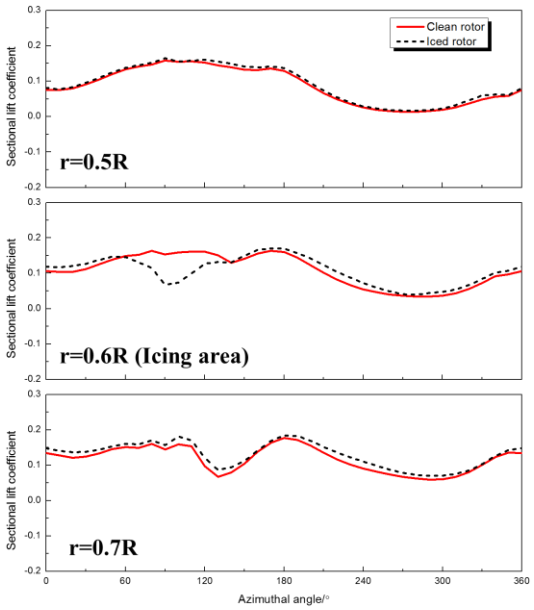

Figure 25. Sectional lift coefficients for the clean and iced rotors

Figure 26 shows comparisons of the effective sound pressure with and without ice on the z=-0.2R plane. Unlike hover, the acoustic characteristics are different around the azimuth.

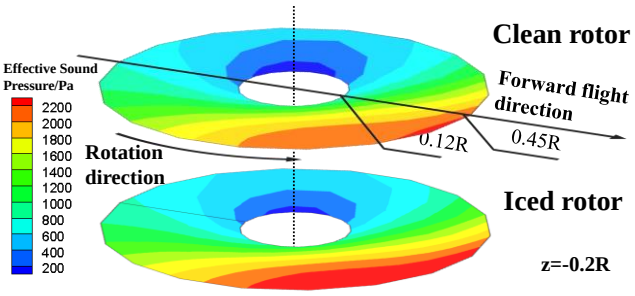

(a) Effective sound pressure on the z=-0.2R plane

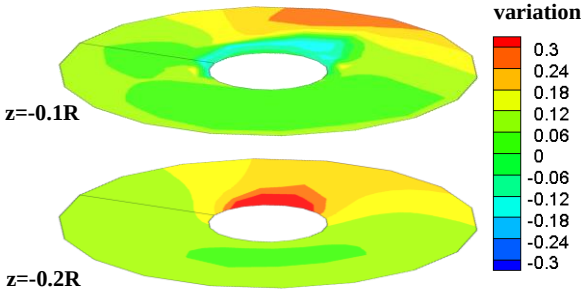

(b) Variation of effective sound pressure

Figure 26. Effective sound pressure of the rotor with and without ice

To be clear, figure 27 shows the effective sound pressure at 0 ° and 180 ° azimuth angles, on the z=-0.1R and z=-0.2R planes. Overall, the difference increases along the radial direction.

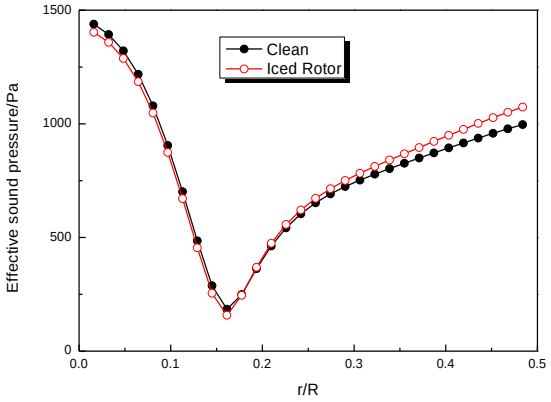

(a) 0 °azimuthal angle, z=-0.1R

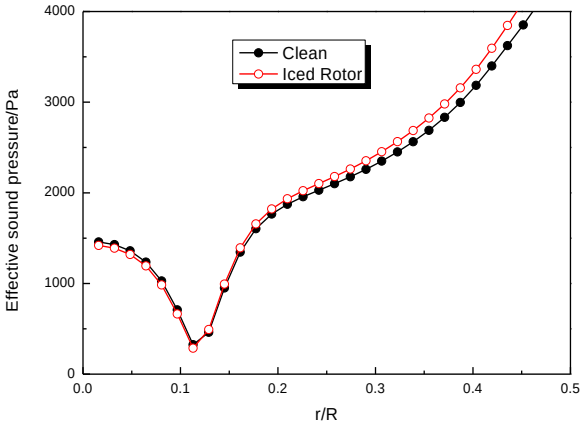

(b) 180 °azimuthal angle, z=-0.1R

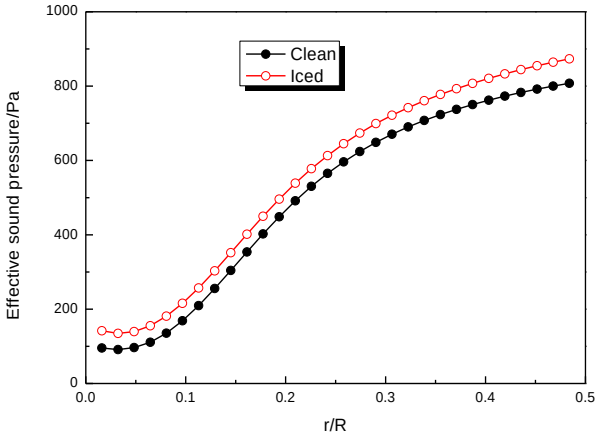

(c) 0 °azimuthal angle, z=-0.2R

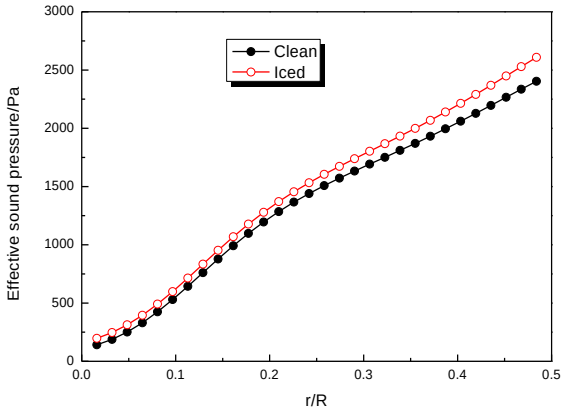

(d) 180 °azimuthal angle, z=-0.2R

Figure 27. Effective sound pressure of the rotor along the radial direction with and without ice

Figure 28 shows the comparison of the total sound pressure time histories at two monitoring positions on the z=-0.2R plane. The differences in sound pressure time histories are obvious, and can be seen by a monitor located on the fuselage.

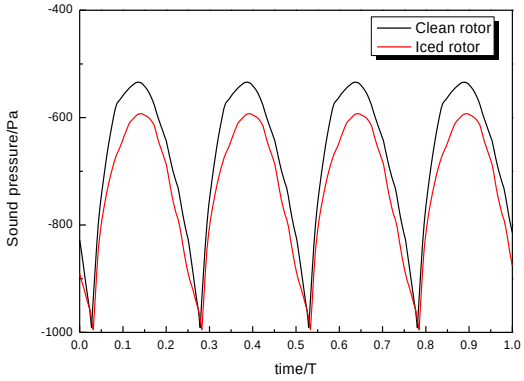

(a) r=0.3R, 0 °azimuthal angle

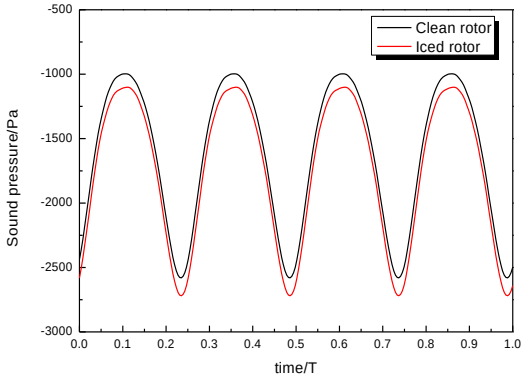

(b) r=0.3R, 180 °azimuthal angle

Figure 28. Comparison of total sound pressure time histories at two monitoring positions on the z=-0.2R plane

CONCLUSIONS

1) Aero-acoustic characteristics of rotors are greatly influenced by ice accretion. Overall, the effect of ice on the acoustics increases with the decrease of the vertical distance of the microphone, and slightly increases with the increase of the radial distance. The variation of the thickness noise will be small if the volume of ice is small.

2) Ice on rotors can be detected at certain microphone positions near the rotor plane. If the ice length is short, the sound pressure will only change in a limited region along the blade radius.

3) If ice is formed near the blade root, the signal captured by monitors near the blade root changes, while that by monitors near the blade tip remains unchanged. Through variations of the sound pressure at different monitoring points, the icing position on the rotor can be detected, especially if several monitors are used.

Author contact:

George Barakos george.barakos@glasgow.ac.uk
Xi Chen chenxicc@nuaa.edu.cn
Qijun Zhao zhaoqijun@nuaa.edu.cn

REFERENCES

[1]Hartman, P., "Prediction of Ice Accumulation and Airfoil Performance Degradation: a Boeing-Cira Research Collaboration," AHS International 62nd Annual Forum, 2006.

[2]Robert, J. F., "Artificial Icing Tests of the S-92 Helicopter in the Mckinley Climatic Laboratory," AIAA 2004-0737, 2004.

[3]Weisend, N. Jr., "Design of an Advanced Pneumatic Deicer for the Composite Rotor Blades," Journal of Aircraft, Vol. 26, (10), 2015, pp. 947-950.

[4]Caliskan, F., Hajiyev, C., "In-flight Detection and Identification and Accommodation of Aircraft Icing," 9th International Conference on Mathematical Problems in Engineering, Aerospace and Sciences, 2012.

[5]Heinrich, A., Ross, R., Zumwait, G., Provorse, J., Padmanabhan, V., Thompson, J., and Riley, J., "Aircraft Icing Handbook, Volumes I-III," Atlantic City International Airport, NJ:FAA technical Center, 1991. DOT/FAA/CT-88/8-1.

[6]Zhao, G. Q., Zhao, Q. J., and Chen, X., "New3-D Ice Accretion Method of Hovering Rotor Including Effects of Centrifugal Force," Aerospace Science and Technology, Vol. 48, Jan. 2016, pp. 122–130.

[7]Wang, Z., Zhu, C., "Study of the Effect of Centrifugal Force on Rotor Blade Icing Process," International Journal of Aerospace Engineering, vol. 2017, Article ID 8695170, 9 pages, 2017. doi:10.1155/2017/8695170.

[8]Dershowitz, A., Hansman, J., "Experimental Investigation of Passive Infrared Ice Detection for Helicopter Applications," 29th Aerospace Sciences Meeting, Reno, NV, USA, 1991.

[9]Melody, J.W., Başar, T., Perkins, W.R., Voulgaris, P.G., "Parameter Identification for Infight Detection and Characterization of Aircraft Icing," Control Engineering Practice, Vol. 8, 2000, pp. 985-1001.

[10]Roy, S., Izad, A., Deanna, R. G., Mehregany, M., "Smart Ice Detection System based on Resonant Piezoelectric Transducer," Sensors & Actuators A Physical, Vol. 69, (3), 1998, pp. 243-250.

[11]Ikiades, A., Howard, G., Armstrong, D., Konstantaki, M., Crossley, S., "Measurement of Optical Diffusion Properties of Ice for Direct Detection Ice Accretion Sensors," Sensors & Actuators A Physical, Vol. 140, (1), 2007, pp. 24-31.

[12]Vellekoop, M. J., Jakoby, B., Bastemeijer, J., "A Love-wave Ice Detector," IEEE Ultrasonics Symposium, 1999, pp. 453-456.

[13]Yin, X., Zhang, Y., Wang, D., "Integration of Self‐Lubrication and Near‐Infrared Photo thermogenesis for Excellent Anti‐Icing/Deicing Performance," Advanced Functional Materials, Vol. 25, (27), 2015,pp. 4237-4245.

[14]Chen, X., Zhao, Q. J., Ma, Y. Y., Wang, B., "Mechanism Analyses on Aeroacoustic Characteristics of Iced Rotor for Ice Detection," AHS International 73nd Annual Forum, 2017.

[15]Chen, X., Zhao, Q., "Numerical Simulations for Ice Accretion on Rotors Using New Three-Dimensional Icing Model," Journal of Aircraft, Vol. 54, (4), 2017, pp. 1428-1442.

[16]Cheng, B. F., Han, Y. Q., Brentner, K. S., "Rotor Broadband Noise due to Surface Roughness during Ice Accretion," AIAA paper 2016-1270, 2016.

[17]Francescantonio, P. D., "A New Boundary Integral Formulation for the Prediction of Sound Radiation," Journal of Sound and Vibration, Vol. 202, (4), 1997, pp. 491-509.

[18]Brentner, K. S., Farassat, F., "Analytical Comparison of the Acoustic Analogy and Kirchhoff Formulation for Moving Surfaces," AIAA Journal, Vol. 36, (8), 1998, pp. 1379-1386.

[19]Barakos, G., Steijl, R., Badcock, K., Brocklehurst, A., "Development of CFD Capability for Full Helicopter Engineering Analysis," in: 31st European Rotorcraft Forum, Florence, Italy, 13-15 September 2005.

[20]Steijl, R., Barakos, G., "CFD Analysis of Complete Helicopter Configurations - Lessons Learnt from the GOAHEAD Project," Aerospace Science and Technology, Vol. 19, 2012, pp. 58-71.

[21]Farassat, F., "Linear Acoustic Formulas for Calculation of Rotating Blade Noise," AIAA Journal, Vol. 19, (9), 1981, pp. 1122-1130.

[22]Bragg, M. B., Broeren, A. P., Blumenthal, L. A., "Iced-airfoil Aerodynamics," Progress in Aerospace Sciences, Vol. 41, 2005, pp. 323-362.

[23]Caradonna, F. X., Laub, G. H., Tung, C., "An Experimental Investigation of the Parallel Blade-vortex Interaction," NASA/TM 86005, 1984.